



Article

Novel Nanoarchitected Cu₂Te as a Photocathodes for Photoelectrochemical Water Splitting Applications

Dong Jin Lee ¹, G. Mohan Kumar ¹, V. Ganesh ², Hee Chang Jeon ¹, Deuk Young Kim ^{1,3}, Tae Won Kang ¹ and P. Ilanchezhiyan ^{1,*}

¹ Quantum-Functional Semiconductor Research Center (QSRC), Institute of Future Technology, Dongguk University, Seoul 04623, Korea

² Department of Physics and Nanotechnology, SRM Institute of Science and Technology, Kattankulathur, Chennai 603203, India

³ Division of Physics and Semiconductor Science, Dongguk University, Seoul 04623, Korea

* Correspondence: ilancheziyan@dongguk.edu

Abstract: Designing photocathodes with nanostructures has been considered a promising way to improve the photoelectrochemical (PEC) water splitting activity. Cu₂Te is one of the promising semiconducting materials for photoelectrochemical water splitting, the performance of Cu₂Te photocathodes remains poor. In this work, we report the preparation of Cu₂Te nanorods (NRs) and vertical nanosheets (NSs) assembled film on Cu foil through a vapor phase epitaxy (VPE) technique. The obtained nano architectures as photocathodes toward photoelectrochemical (PEC) performance was tested afterwards for the first time. Optimized Cu₂Te NRs and NSs photocathodes showed significant photocurrent density up to 0.53 mA cm⁻² and excellent stability under illumination. Electrochemical impedance spectroscopy and Mott–Schottky analysis were used to analyze in more detail the performance of Cu₂Te NRs and NSs photocathodes. From these analyses, we propose that Cu₂Te NRs and NSs photocathodes are potential candidate materials for use in solar water splitting.

Keywords: copper telluride; nanorods; nanosheets; photocathodes; PEC water splitting



Citation: Lee, D.J.; Mohan Kumar, G.; Ganesh, V.; Jeon, H.C.; Kim, D.Y.; Kang, T.W.; Ilanchezhiyan, P. Novel Nanoarchitected Cu₂Te as a Photocathodes for Photoelectrochemical Water Splitting Applications. *Nanomaterials* **2022**, *12*, 3192. <https://doi.org/10.3390/nano12183192>

Academic Editor: Yuichi Negishi

Received: 2 August 2022

Accepted: 8 September 2022

Published: 14 September 2022

Publisher's Note: MDPI stays neutral with regard to jurisdictional claims in published maps and institutional affiliations.



Copyright: © 2022 by the authors. Licensee MDPI, Basel, Switzerland. This article is an open access article distributed under the terms and conditions of the Creative Commons Attribution (CC BY) license (<https://creativecommons.org/licenses/by/4.0/>).

1. Introduction

Photoelectrochemical (PEC) water splitting has been regarded as attractive technology because it provides sustainable and alternative source of energy [1–4]. Semiconductor electrodes play a vital role for efficient solar water splitting to produce clean and renewable H₂ and O₂ [5,6]. Designing semiconductor photoelectrodes with suitable band edge energies that function as energy converters, photosensitizers, and have good photostability, is of fundamental importance. Silicon showed great promise as a photocathode material due to its band gap and earth abundance. However, it suffers from drawbacks such as high reflectivity, limited photovoltage, sluggish reaction kinetics, and photocorrosion in aqueous solution [7–9]. Research from several groups has investigated photocathode materials based on transition metal chalcogenides [10,11], phosphides [12,13], oxides [14,15], Sb₂Se₃ [16], CdTe [17], and SnS [18]. However, their performance and chemical stability needs to be improved. It is still a significant challenge in developing an ideal photocathode material with long-term stability and high efficiency for practical applications.

Recently copper chalcogenides have gained considerable attention owing to their wide range of phases and compositions, which allows them to tune their physical and chemical properties for a diverse range of applications [19–24]. Among them, copper telluride (Cu₂Te), a p-type semiconductor has gained considerable interest for its potential application in solar cells [25], memory devices [26], lithium ion batteries [27], and thermoelectric materials [28]. In the past, studies on Cu₂Te were mainly on their thermoelectric and electrical properties. Applications of Cu₂Te materials in PEC water splitting have been seldomly explored. For example, Sangeetha et al., studied the electrocatalytic water

reduction of Cu_{2-x}Te by tuning Cu overvoltage. The catalyst shows a low overpotential of 347 mV at 10 mA cm^{-2} towards the HER [29]. On the other hand, Ghosh et al., reported electrochemically deposited Cu_7Te_4 thin films to degrade organic pollutant dyes under visible light irradiation. The Cu_7Te_4 thin film showed superior photoactivity to reduce toxic Cr(VI) to Cr(III) and the effective removal of Cr(VI) up to 99.8% in 30 min [30]. More recently, Cu_7Te_4 nanosheet was prepared by Wang et al., for OER activity and showed a low overpotential of 323 mV to drive the current density of 10 mA cm^{-2} and a small Tafel slope of 86 mV dec^{-1} [31].

Inspired by these, we report the direct synthesis of Cu_2Te NRs and vertical NSs on Cu foil via VPE. In addition, there have been no reports on the preparation of one-dimensional (1D) and two-dimensional (2D) like Cu_2Te (e.g., nanorods and vertical nanosheets) by utilizing Cu foil as both substrate and Cu resource. The structural and morphological properties of as-synthesized Cu_2Te nanostructures were systematically assessed. The as-prepared Cu_2Te nanostructured samples were then utilized as the photocathode for studying the PEC properties under illumination for the first time. The photocathode based on vertical NSs exhibits excellent PEC performance compared to NRs. The enhanced performance can be due to a large surface area and more active sites, which can provide a high interfacial contact between the electrolytes for fast interfacial charge transfer.

2. Experimental Section

Preparation of Cu_2Te Nanostructures

The 1D and 2D Cu_2Te nanostructures were grown via a VPE system used in previous studies [32,33]. Tellurium (Te) powder as chemical precursor, and Cu foil as the substrate, were chosen for the deposition of Cu_2Te nanostructures. In the Cu_2Te growth process, 0.5 g high purity (99.999%) Te source is placed in the source zone of the VPE-chamber and Cu substrate were placed 10 cm away from the Te source in the downstream direction. Before flowing the gas, the initial chamber was evacuated to a vacuum of 2×10^{-3} Torr using a rotary pump. The quartz chamber was purged with N_2 gas (200 sccm) and then sufficiently flowed for 10 min to remove residual oxygen and then carrier N_2 gas was maintained at 50 sccm. In all growth processes, the growth time was 30 min, the temperature of the source zone was maintained at $700 \text{ }^\circ\text{C}$, and the operating pressure at this time was 3.5×10^{-1} Torr. The growth time is 30 min. For the production of different nanostructures, the growth temperature of Cu_2Te was set at $550 \text{ }^\circ\text{C}$ for nanorods and $600 \text{ }^\circ\text{C}$ for nanosheets, respectively, and carrier N_2 gas was maintained at 50 sccm. More details about the characterization techniques and photoelectrochemical measurements are described in the Supplementary Information (SI).

3. Results and Discussions

Cu_2Te nanostructured film was synthesized via a vapor phase epitaxy (VPE) route from the reaction of Te powder and Cu foil. Figure 1a presents the schematic of the fabrication process of Cu_2Te nanostructured film prepared on the Cu foil. From the Figure 1, it can be seen that Te powders placed at the source zone of the quartz tube and Cu foil placed at the downstream direction. When the growth temperature is reached, Te powders were evaporated, carried by N_2 gas will react with the Cu foil substrate at $550 \text{ }^\circ\text{C}$ and $600 \text{ }^\circ\text{C}$ to form into Cu_2Te NRs and vertical NSs films (detailed synthesis processes are provided in the experimental section). The surface morphologies of as deposited Cu_2Te nanostructured films were studied by FESEM technique. Figure 1b,c displays the SEM images of the as-prepared film on the surface of Cu foil at $550 \text{ }^\circ\text{C}$, showing the deposition of numerous NRs on the whole Cu foil. Typical NRs have length of $\sim 1 \text{ } \mu\text{m}$ as can be seen in the cross-sectional SEM image (Figure 1d). Similarly, the SEM images (Figure 1e,f) show vertically aligned NSs morphologies on Cu foil deposited at $600 \text{ }^\circ\text{C}$ with uniform distribution. Moreover, the vertical Cu_2Te NSs arrays with a thickness of several hundred nanometers randomly extended can be observed from the cross-sectional SEM image in Figure 1g.

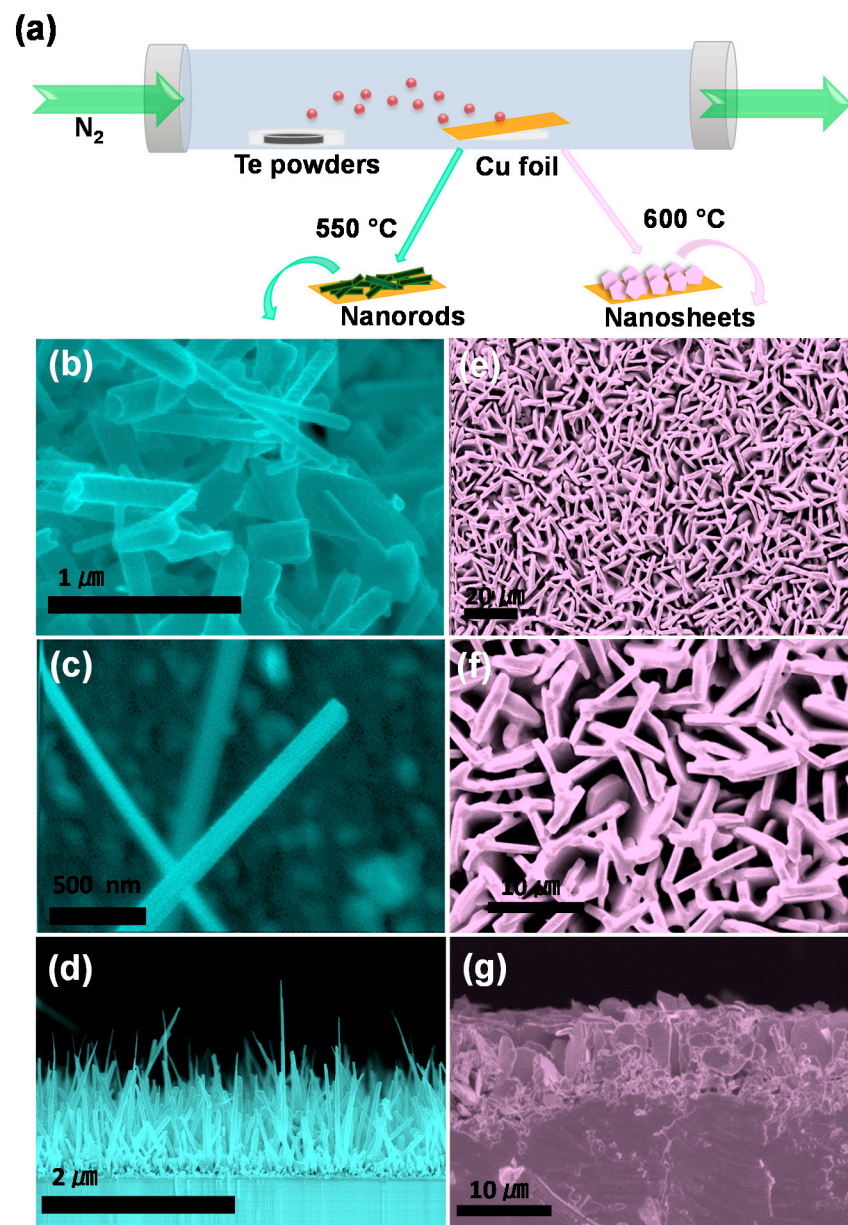


Figure 1. Sample preparation and morphology characterization. (a) Schematic of the fabrication process of Cu₂Te nanostructured film prepared on the Cu foil. (b,c) SEM and (d) cross section image of Cu₂Te NRs and (e,f) SEM and (g) cross section image of Cu₂Te NSs.

The morphologies of Cu₂Te nanostructured films were further studied by high resolution transmission electron microscopic (HRTEM) techniques as shown in Figure 2. The TEM images in Figure 2a,c further demonstrate the NRs and NSs morphology. The clearly resolved lattice fringe is measured to be about 0.359 nm for both the nanostructures, corresponding well to the (211) plane of Cu₂Te.

The phase structure of as-synthesized Cu₂Te NRs and NSs films, were investigated through XRD patterns as depicted in Figure 3a. Here, several diffraction peaks were observed for both Cu₂Te NRs and NSs films, which can be assigned to orthorhombic Cu₂Te (PDF # 00-037-1027). The diffraction peaks can be indexed as (031), (211), (222), and (0118) planes of Cu₂Te. More specifically, both the films show a predominant peak at 24.7°, which indicates that the (211) plane is highly preferred, which is in agreement with HRTEM image. Apart from Cu₂Te peaks, the two Cu (111) and (200) peaks were seen in the diffraction pattern, which are related to Cu foil.

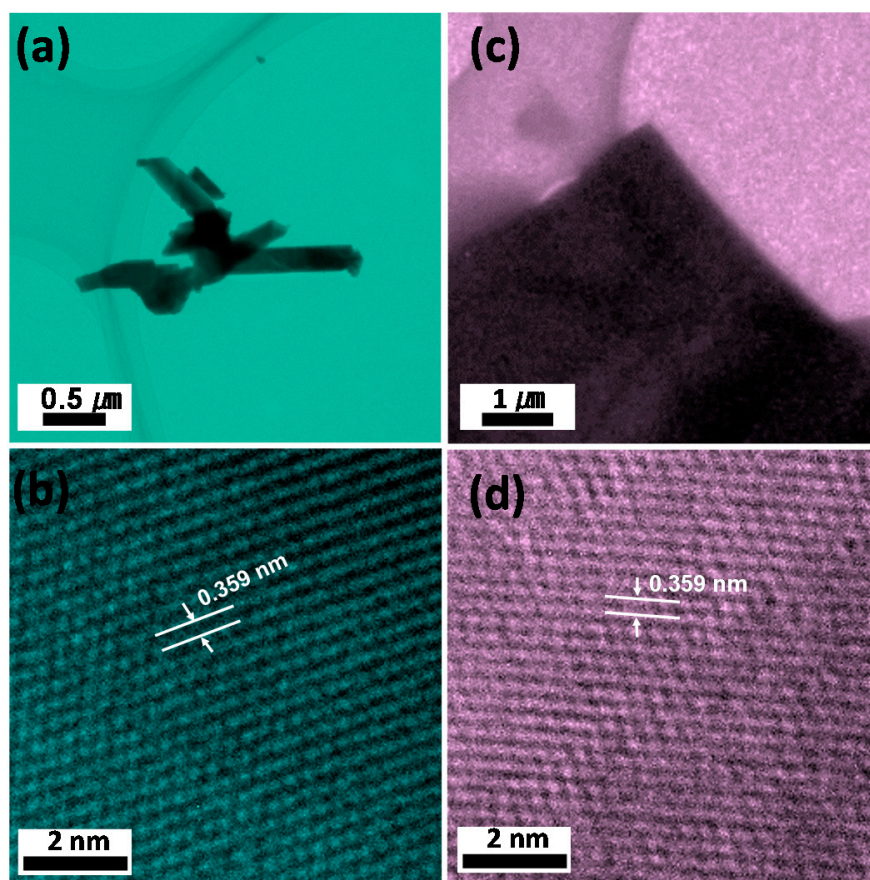


Figure 2. TEM images (a,c) and HRTEM image (b,d) of Cu_2Te NRs and vertical NSs.

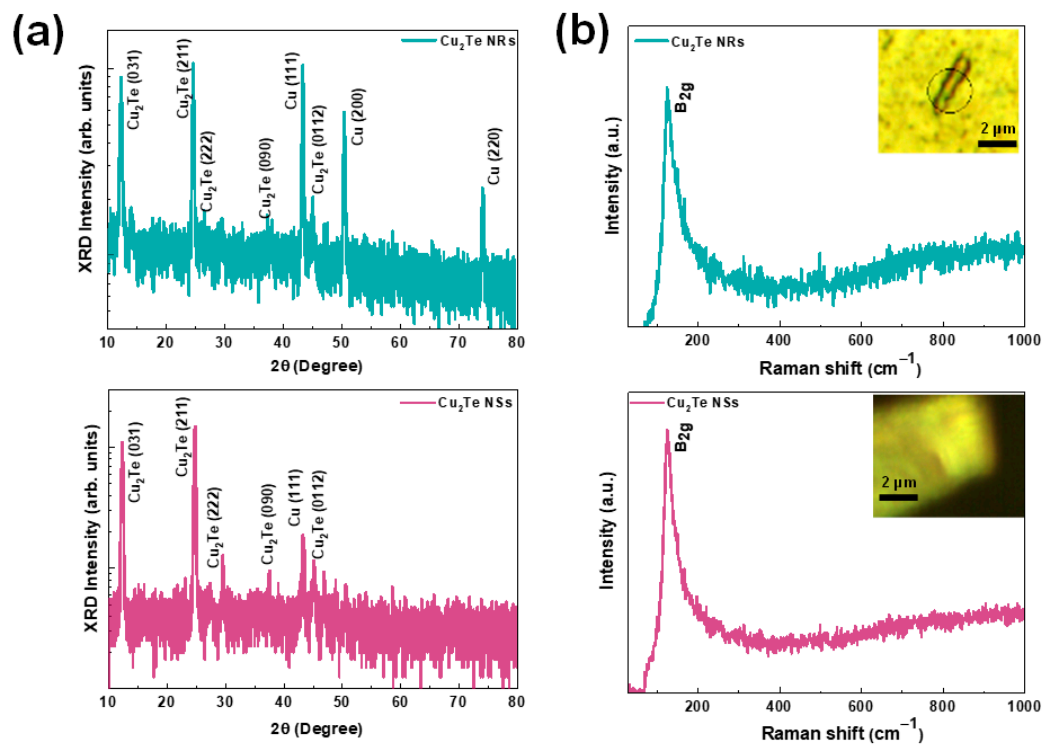


Figure 3. X-ray diffraction pattern of (a) Cu_2Te NRs and vertical NSs and (b) Raman spectrum of Cu_2Te NRs and vertical NSs. Inset shows the optical micrograph image of studied NRs and NSs.

To further study the structural properties of the Cu_2Te NRs and vertical NSs, Raman spectroscopy was employed. Figure 3b displays typical Raman spectra of Cu_2Te NRs and vertical NSs. The image inset shows the optical micrograph image of studied NRs and NSs. Upon 532 nm laser excitation, both the Raman spectrum of NRs and vertical NSs exhibits a sharp peak positioned at 123 cm^{-1} , which agrees with the data previously reported for Cu_2Te [34]. The observed peak has been assigned to B_{2g} vibration mode of Cu_2Te phase [35,36]. The absence of oxidation-related peaks indicates high quality of the synthesized Cu_2Te samples.

X-ray photoelectron spectroscopy (XPS) was adopted to provide information about the chemical bonding and elemental composition in as-grown Cu_2Te NRs and NSs films. The full survey XPS scan of Cu_2Te NRs and vertical NSs with element denotation are shown in Figure 4a. The XPS core level spectra of Cu 2p of NRs and NSs films (Figure 4b) show two strong peaks from Cu $2p_{1/2}$ and Cu $2p_{3/2}$. As represented by Gaussian fitting, the core level spectra of Cu 2p confirm the presence of Cu^{1+} and Cu^{2+} in both NRs and vertical NSs. The peaks appeared at 932.4 eV (Cu $2p_{3/2}$) and 952.3 eV (Cu $2p_{1/2}$) are assigned to Cu^{1+} . Similarly, the peaks at 933.6 eV (Cu $2p_{3/2}$) and 952.9 eV (Cu $2p_{1/2}$) are the typical values for Cu^{2+} , of Cu_2Te , respectively [37,38]. Additionally, two weak satellite features could be observed at 944.1 eV and 962.4 eV, respectively, and is also attributed to Cu^{2+} . This is possibly attributed to the unavoidable surface oxidation under air atmosphere. The XPS core level spectra of Te (Figure 4c) in both NRs and vertical NSs have peaks at binding energies of 583.1 eV, corresponding to Te^{2-} states of Cu_2Te , respectively [39].

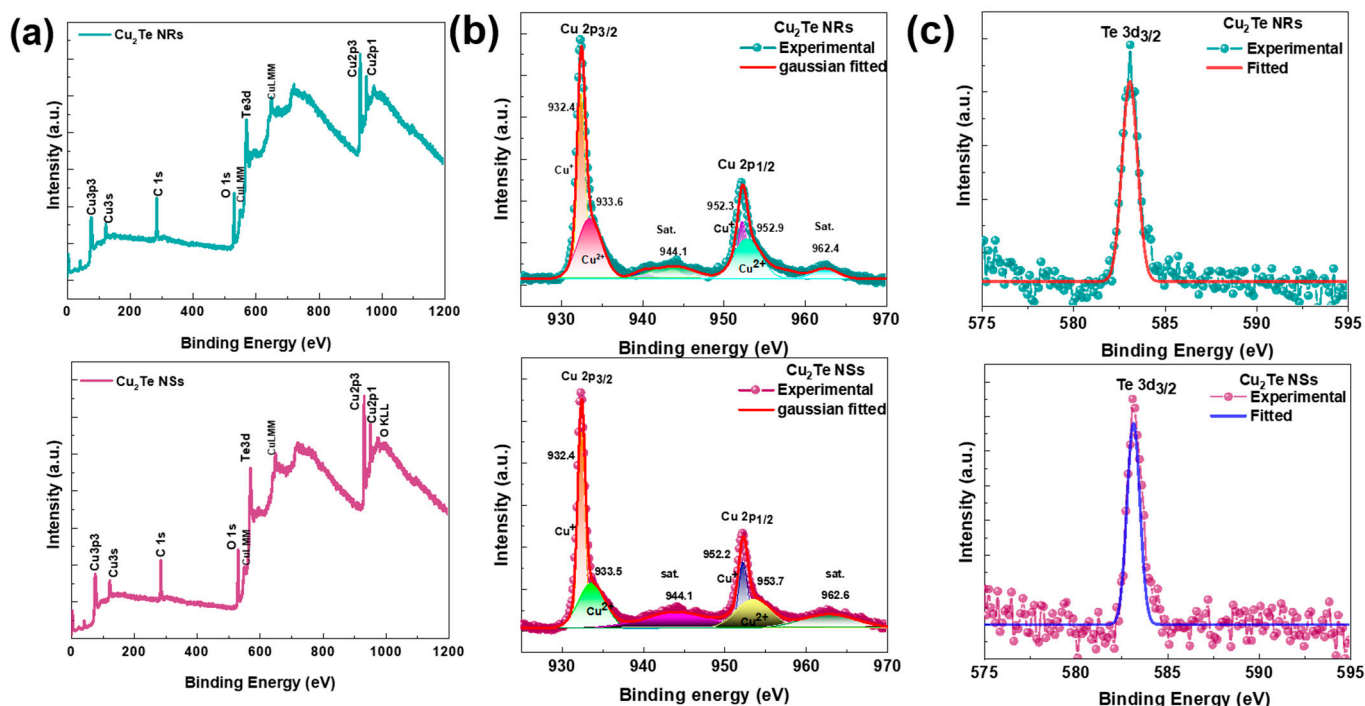


Figure 4. (a) Full scan survey spectrum Cu_2Te NRs and NSs. (b) high-resolution spectra of Cu 2p and (c) Te 3d of Cu_2Te NRs and NSs.

Furthermore, the tellurium-to-copper stoichiometric ratio of Te and Cu of approximately 1:2 is obtained for both the NRs and NSs from the XPS, suggesting grown Cu_2Te is chemically stoichiometric. The results above demonstrate the successful synthesis of Cu_2Te on a copper foil.

The PEC performances of the Cu_2Te nanostructured photocathodes were acquired by linear sweep voltammetry (LSV) measurements under dark and light conditions (100 mW cm^{-2}) in $0.5\text{ M Na}_2\text{SO}_4$ electrolyte. The photocurrent-density variations for both Cu_2Te NRs and NSs photocathodes are illustrated in Figure 5a. As observed from Figure 5a, both

the samples reveal obvious photocurrent under illumination, demonstrating the efficient charge transfer process at semiconductor/electrolyte interfaces. Besides, the photocurrent density increases with increasing applied potential in the negative direction, implying the p-type conductivity and could possibly be employed as a photocathode material for water splitting. At a bias potential of -0.5 V, the Cu_2Te NRs photocathodes generate a photocurrent density of 0.21 mA cm^{-2} . Interestingly, the photocurrent density of Cu_2Te vertical NSs photocathodes reached the maximum value of 0.53 mA cm^{-2} . The enhanced photocurrent density of the vertical NSs can be ascribed to light absorption utilization via multiple reflections of this vertical structure as well as forming intimate contact with the Cu substrate. Moreover, this vertical NSs architecture with an open morphology, provides more active sites, which can provide a high interfacial contact between the electrolytes for fast interfacial charge transfer, thus improving the PEC performance. According to the reported literature, the observed photocurrent density was quite high (Table S1). The generated maximum photocurrent density was ~ 2 -times higher compared to that of NRs. However, in this study, the photocurrent value of the photocathodes is closely related to the morphological properties of the films.

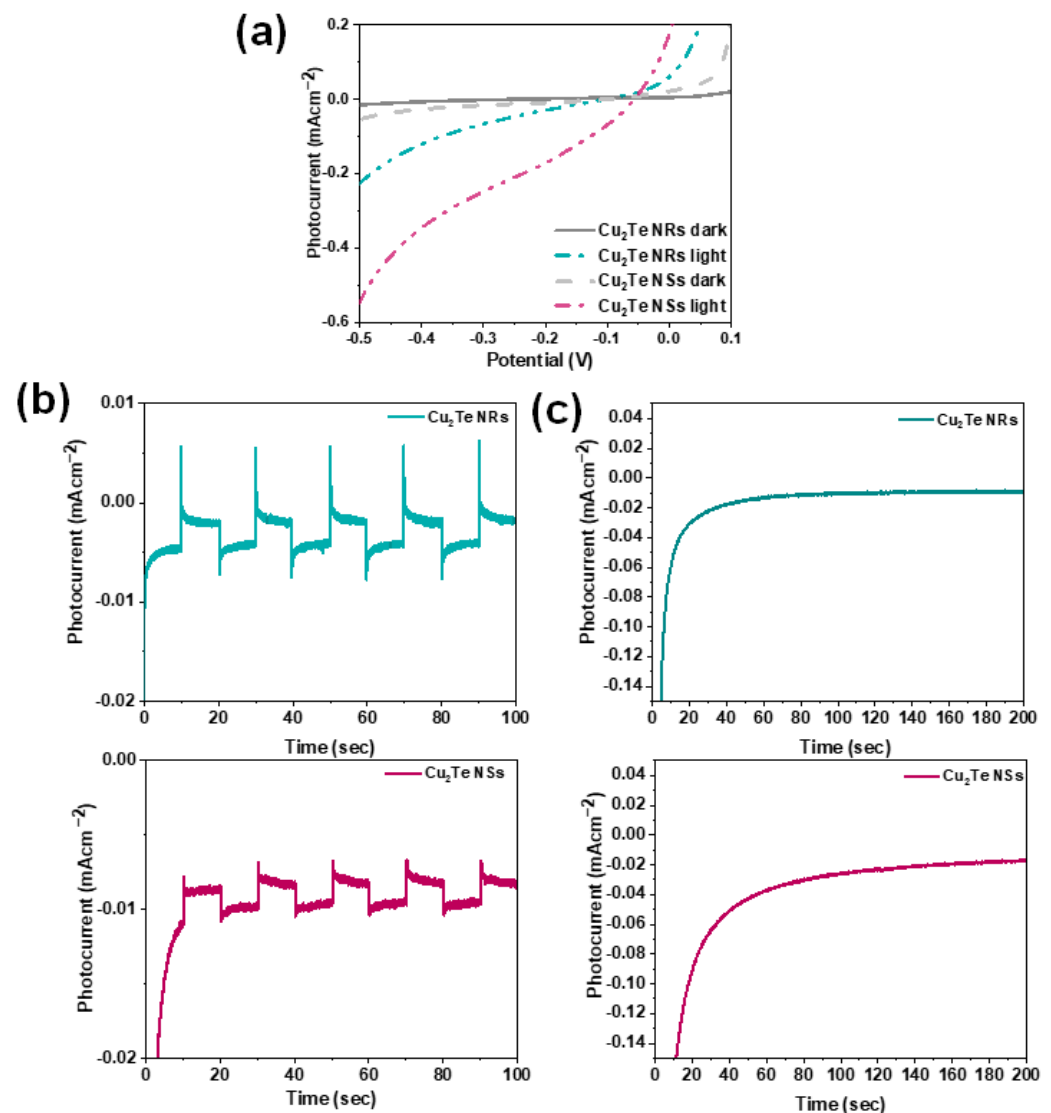


Figure 5. (a) Photocurrent density versus voltage curves of Cu_2Te NRs vertical NSs photocathodes. (b) Photocurrent density versus time ($I-t$) curves of Cu_2Te NRs and vertical NSs. (c) Photostability curve of the Cu_2Te NRs and vertical NSs.

The chronoamperometric I-t curves examining the photocurrent of the Cu₂Te NRs and vertical NSs photocathodes under chopped illuminations are shown in Figure 5b. The photocurrent of both NRs and NSs exhibits a prompt rise under each illumination, and quickly drops when the light is turned off, demonstrating the excellent switching behavior and good stability of the photocathodes. Afterward, a photostability test for the Cu₂Te NRs and vertical NSs (Figure 5c) photocathodes was carried out under continuous illumination and displayed a good stability. Both the photocathodes nearly maintained 70% retention of initial value after 200 s suggesting the excellent stability. Finally, to give more evidence, we also performed XRD measurements for the photocathodes after the PEC stability test. As can be observed from Figure S1, it is worth mentioning that predominant peak at 24.7° appears in the XRD pattern of both Cu₂Te NRs and vertical NSs photocathodes after the stability test demonstrates its excellent structural stabilities. The above results highlight the promising potential of the Cu₂Te NSs and NRs as state-of-the art photocathodes.

The PEC performance of Cu₂Te NRs and vertical NSs photocathodes was further studied with (EIS) under light illumination. This investigation was made in order to elucidate the charge transfer resistance at the photocathode/solution interface. Figure 6a presents the typical Nyquist curves of Cu₂Te NRs and vertical NSs photocathodes under illumination. As seen from Figure 6a, both the Nyquist curves show a semicircle arc at high frequency can be used to identify charge transfer resistance and a straight line at low-frequency regions (mass transfer). The fitted equivalent circuit model for the photocathodes is given in Figure 6b, where R_{ct}, R_s, CPE, and W_Z represents charge transfer resistance, electrolyte resistance, constant phase element, and Warburg impedance. The values obtained from the fitted circuit are summarized in Table S2. The charge transfer resistance from Cu₂Te NSs were found to be systematically decreased as compared with Cu₂Te NRs. These results suggest that the Cu₂Te NSs could offer smoother carrier diffusion paths and, hence, higher photoelectrochemical performances compared with the Cu₂Te NRs. The PEC behavior of the photocathodes was then examined with the log |Z| vs. log frequency (log f) plots in Figure 6c. The vertical NSs photocathodes display minimum |Z| compared to the NRs photocathodes indicating its higher PEC activity. Figure 6d reveals the phase angle vs. log f plots. Here, the Cu₂Te NRs photocathodes showed a high phase angle around (−75°), while NSs photocathodes exhibits phase angle around (−60°). The less-negative phase angle for the Cu₂Te NSs in comparison to NRs photocathodes further confirmed a lower resistance to charge mobility in the semiconductor and at the electrolyte/photocathode interface. Additionally, the characteristic peak frequency shifted to a low value for NSs photocathode, indicating it has longer carrier lifetime than in NRs photocathode and thus a lower recombination rate.

Finally, Mott–Schottky (M-S) analysis was employed to estimate charge carrier density (N_A) and flat band potential (V_{fb}) of the Cu₂Te NRs and NSs photocathodes. Figure 7a,b illustrates the Mott–Schottky plots (1/C² as a function of applied potential) measured at a frequency of 1000 Hz. The negative slope of the plots indicated that both Cu₂Te NRs and vertical NSs are p-type semiconductors. Furthermore, the flat band potentials of Cu₂Te NRs and vertical NSs was determined to be 0.25 V and 0.28 V by extrapolating the X intercepts in Mott–Schottky plots. Additionally, the carrier density N_A was estimated from Figure 7 using the following equation [40]:

$$N_A = (2/e\epsilon\epsilon_0) (d(1/C^2)/dV)^{-1}$$

where e is the elemental charge, ϵ the dielectric constant of Cu₂Te (taken as 17) [41], ϵ_0 the permittivity of vacuum, N_A is the concentration of charge carriers, and C is the space charge layer capacitance. According to the equation and Figure 7, the N_A value of the Cu₂Te NRs and NSs were determined to be 3.35×10^{18} and 4.3×10^{18} cm^{−3}. Evidently, the higher carrier density in the case of vertical NSs and charge transfer efficiency have contributed to the enhanced PEC performance.

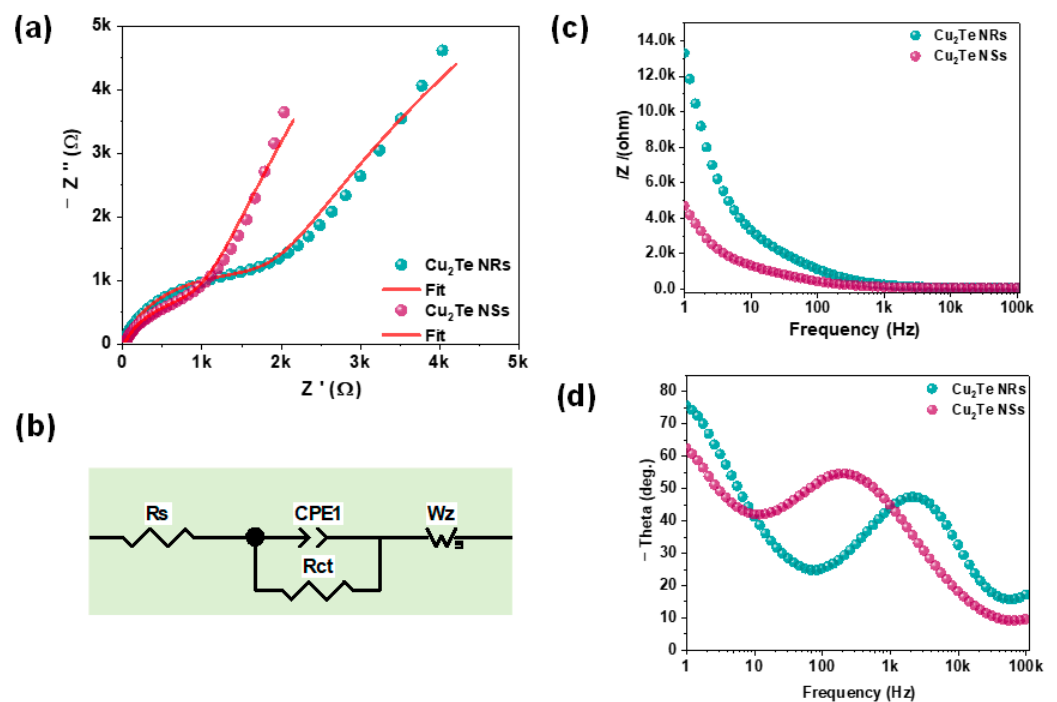


Figure 6. (a) Nyquist plots of the Cu_2Te NRs and vertical NSs. (b) Shows the fitted equivalent circuit. (c) Bode and (d) Phase angle plots of Cu_2Te NRs and NSs.

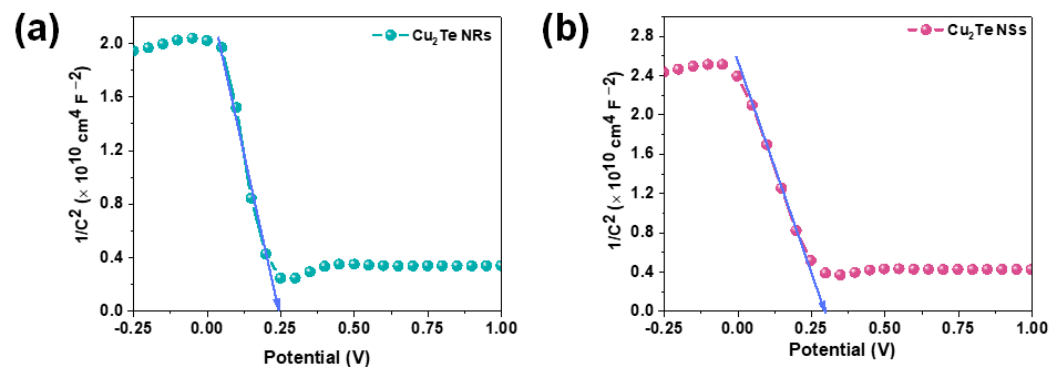


Figure 7. Mott-Schottky plot of (a) Cu_2Te NRs and (b) vertical NSs.

4. Conclusions

In summary, we presented a synthesis of Cu_2Te NRs and vertical NSs assembled film on Cu foil as photocathodes in a water splitting PEC. The morphological and microstructural properties and chemical states of the Cu_2Te were systematically discussed. It is worth mentioning that the Cu_2Te NRs and vertical NSs delivered unique photoelectrochemical performances. Compared with NRs, vertical NSs photocathodes exhibited higher photocurrent density. EIS results revealed excellent performance of Cu_2Te NSs photocathodes, which can be ascribed to low charge transfer resistances across electrolyte/electrode interfaces. We believe that the above results reported herein will open a new avenue in the development of Cu_2Te -based photocathodes for efficient PEC water splitting.

Supplementary Materials: The following supporting information can be downloaded at: <https://www.mdpi.com/article/10.3390/nano12183192/s1>, Figure S1: X-ray diffraction pattern of Cu_2Te NRs and vertical NSs after stability test; Table S1: A comparisons of PEC performances of Cu_2Te photocathodes is given below; Table S2: Various parameters extracted from the equivalent circuit fit to the EIS data for Cu_2Te NRs and NSs photocathodes in 0.5M Na_2SO_4 electrolyte solutions [42–46].

Author Contributions: Conceptualization, D.J.L., G.M.K. and P.I.; Data curation, D.J.L., H.C.J. and V.G.; Supervision, T.W.K. and D.Y.K.; Validation, G.M.K. and P.I.; Visualization, T.W.K. and D.Y.K.; Writing—original draft, P.I. All authors have read and agreed to the published version of the manuscript.

Funding: This research was funded by the National Research Foundation of Korea (NRF) grant funded by the Korea government (MSIT) (no. 2022R1F1A1066650, 2021R1F1A1045642 and 2016R1A6A1A03012877).

Data Availability Statement: Not applicable.

Conflicts of Interest: The authors declare no conflict of interest.

References

1. Ager, J.W.; Shaner, M.R.; Walczak, K.A.; Sharp, I.D.; Ardo, S. Experimental Demonstrations of Spontaneous, Solar-Driven Photoelectrochemical Water Splitting. *Energy Environ. Sci.* **2015**, *8*, 2811–2824. [[CrossRef](#)]
2. Ding, Q.; Meng, F.; English, C.R.; Cabaán-Acevedo, M.; Shearer, M.J.; Liang, D.; Daniel, A.S.; Hamers, R.J.; Jin, S. Efficient Photoelectrochemical Hydrogen Generation Using Heterostructures of Si and Chemically Exfoliated Metallic MoS₂. *J. Am. Chem. Soc.* **2014**, *136*, 8504–8507. [[CrossRef](#)] [[PubMed](#)]
3. Edwards, P.P.; Kuznetsov, V.L.; David, W.I.F.; Brandon, N.P. Hydrogen and Fuel Cells: Towards a Sustainable Energy Future. *Energy Policy* **2008**, *36*, 4356–4362. [[CrossRef](#)]
4. McKone, J.R.; Lewis, N.S.; Gray, H.B. Will Solar-Driven Water-Splitting Devices See the Light of Day? *Chem. Mater.* **2014**, *26*, 407–411. [[CrossRef](#)]
5. Osterloh, F.E. Inorganic nanostructures for photoelectrochemical and photocatalytic water splitting. *Chem. Soc. Rev.* **2013**, *42*, 2294–2320. [[CrossRef](#)]
6. Maeda, K. Photocatalytic water splitting using semiconductor particles: History and recent developments. *J. Photochem. Photobiol. C Photochem. Rev.* **2011**, *12*, 237–268. [[CrossRef](#)]
7. Fominski, V.; Demin, M.; Fominski, D.; Romanov, R.; Rubinkovskaya, O.; Shvets, P.; Goikhman, A. Pulsed Laser Phosphorus Doping and Nanocomposite Catalysts Deposition in Forming α -MoS_x/NP-Mo/ $n+p$ -Si Photocathodes for Efficient Solar Hydrogen Production. *Nanomaterials* **2022**, *12*, 2080. [[CrossRef](#)]
8. Cheng, C.; Zhang, W.; Chen, X.; Peng, S.; Li, Y. Strategies for improving photoelectrochemical water splitting performance of Si-based electrodes. *Energy Sci. Eng.* **2022**, *10*, 1526–1543. [[CrossRef](#)]
9. Benck, J.D.; Lee, S.C.; Fong, K.D.; Kibsgaard, J.; Sinclair, R.; Jaramillo, T.F. Designing Active and Stable Silicon Photocathodes for Solar Hydrogen Production Using Molybdenum Sulfide Nanomaterials. *Adv. Energy Mater.* **2014**, *4*, 1400739. [[CrossRef](#)]
10. Li, C.; Cao, Q.; Wang, F.; Xiao, Y.; Li, Y.; Delaunay, J.-J.; Zhu, H. Engineering graphene and TMDs based van der Waals heterostructures for photovoltaic and photoelectrochemical solar energy conversion. *Chem. Soc. Rev.* **2018**, *47*, 4981–5037. [[CrossRef](#)]
11. Xiao, J.; Zhang, Y.; Chen, H.; Xu, N.; Deng, S. Enhanced Performance of a Monolayer MoS₂/WSe₂ Heterojunction as a Photoelectrochemical Cathode. *Nano-Micro Lett.* **2018**, *10*, 60. [[CrossRef](#)] [[PubMed](#)]
12. Cao, Q.; Hao, S.; Wu, Y.; Pei, K.; You, W.; Che, R. Interfacial charge redistribution in interconnected network of Ni₂P–Co₂P boosting electrocatalytic hydrogen evolution in both acidic and alkaline conditions. *Chem. Eng. J.* **2021**, *424*, 130444. [[CrossRef](#)]
13. Lee, M.H.; Takei, K.; Zhang, J.; Kapadia, R.; Zheng, M.; Chen, Y.-Z.; Nah, J.; Matthews, T.S.; Chueh, Y.-L.; Ager, J.W.; et al. p-Type InP Nanopillar Photocathodes for Efficient Solar-Driven Hydrogen Production. *Angew. Chem. Int. Ed.* **2012**, *51*, 10760–10764. [[CrossRef](#)] [[PubMed](#)]
14. Sekizawa, K.; Oh-ishi, K.; Morikawa, T. Photoelectrochemical water-splitting over a surface modified p-type Cr₂O₃ photocathode. *Dalton Trans.* **2020**, *49*, 659–666. [[CrossRef](#)]
15. Wheeler, G.P.; Choi, K.-S. Investigation of p-type Ca₂Fe₂O₅ as a Photocathode for Use in a Water Splitting Photoelectrochemical Cell. *ACS Appl. Energy Mater.* **2018**, *1*, 4917–4923. [[CrossRef](#)]
16. Lee, H.; Yang, W.; Tan, J.; Oh, Y.; Park, J.; Moon, J. Cu-doped NiO_x as an Effective Hole-Selective Layer for a High-Performance Sb₂Se₃ Photocathode for Photoelectrochemical Water Splitting. *ACS Energy Lett.* **2019**, *4*, 995–1003. [[CrossRef](#)]
17. Ohashi, K.; Uosaki, K.; Bockris, J.O.M. Cathodes for photodriven hydrogen generators: ZnTe and CdTe. *Int. J. Energy Res.* **1977**, *1*, 25–30. [[CrossRef](#)]
18. Lee, H.; Yang, W.; Tan, J.; Park, J.; Shim, S.G.; Park, Y.S.; Yun, J.W.; Kim, K.M.; Moon, J. High-Performance Phase-Pure SnS Photocathodes for Photoelectrochemical Water Splitting Obtained via Molecular Ink-Derived Seed-Assisted Growth of Nanoplates. *ACS Appl. Mater. Interfaces* **2020**, *12*, 15155–15166. [[CrossRef](#)]
19. Yue, J.L.; Sun, Q.; Fu, Z.W. Cu₂Se with Facile Synthesis as a Cathode Material for Rechargeable Sodium Batteries. *Chem. Commun.* **2013**, *49*, 5868–5870. [[CrossRef](#)]
20. Wang, Y.; Feng, X.; Feng, X.; Xiong, Y.; Stoupin, S.; Huang, R.; Zhao, M.; Xu, M.; Zhang, P.; Zhao, J.; et al. An Innovative Lithium Ion Battery System Based on a Cu₂S Anode Material. *ACS Appl. Mater. Interfaces* **2020**, *12*, 17396–17405. [[CrossRef](#)]
21. Li, H.; Jiang, J.; Wang, F.; Huang, J.; Wang, Y.; Zhang, Y.; Zhao, J. Facile Synthesis of Rod-like Cu_{2-x}Se and Insight into its Improved Lithium-Storage Property. *ChemSusChem* **2017**, *10*, 2235–2241. [[CrossRef](#)] [[PubMed](#)]

22. Yang, H.J.; Chen, C.Y.; Yuan, F.W.; Tuan, H.Y. Designed Synthesis of Solid and Hollow Cu_{2-x}Te Nanocrystals with Tunable Near-Infrared Localized Surface Plasmon Resonance. *J. Phys. Chem. C* **2013**, *117*, 21955–21964. [[CrossRef](#)]
23. Bao, H.; Zhang, H.; Zhou, L.; Fu, H.; Liu, G.; Li, Y.; Cai, W. Large Area $\alpha\text{-Cu}_2\text{S}$ Particle-Stacked Nanorod Arrays by Laser Ablation in Liquid and Their Strong Structurally Enhanced and Stable Visible Photoelectric Performances. *ACS Appl. Mater. Interfaces* **2018**, *10*, 19027–19036. [[CrossRef](#)] [[PubMed](#)]
24. Sarkar, S.S.; Bera, S.; Hassan, M.S.; Sapra, S.; Khatri, R.K.; Ray, S.K. $\text{MoSe}_2\text{-Cu}_{2-x}\text{S}/\text{GaAs}$ Heterostructure-Based Self-Biased Two Color-Band Photodetectors with High Detectivity. *J. Phys. Chem. C* **2021**, *125*, 10768–10776. [[CrossRef](#)]
25. Zhou, J.; Wu, X.; Duda, A.; Teeter, G.; Demtsu, S. The Formation of Different Phases of Cu_xTe and Their Effects on CdTe/CdS Solar Cells. *Thin Film Solids* **2007**, *515*, 7364–7369. [[CrossRef](#)]
26. Devulder, W.; Opsomer, K.; Seidel, F.; Belmonte, A.; Muller, R.; Schutter, B.D.; Bender, H.; Vandervorst, W.; Elshocht, S.V.; Jurczak, M.; et al. Influence of Carbon Alloying on the Thermal Stability and Resistive Switching Behavior of Copper-Telluride Based CBRAM Cells. *ACS Appl. Mater. Interfaces* **2013**, *5*, 6984–6989. [[CrossRef](#)]
27. Han, C.; Li, Z.; Li, W.J.; Chou, S.L.; Dou, S.X. Controlled Synthesis of Copper Telluride Nanostructures for Long-Cycling Anodes in Lithium Ion Batteries. *J. Mater. Chem. A* **2014**, *2*, 11683–11690. [[CrossRef](#)]
28. Yao, Y.; Zhang, B.P.; Pei, J.; Sun, Q.; Nie, G.; Zhang, W.Z.; Zhuo, Z.T.; Zhou, W. High Thermoelectric Figure of Merit Achieved in $\text{Cu}_2\text{S}_{1-x}\text{Te}_x$ Alloys Synthesized by Mechanical Alloying and Spark Plasma Sintering. *ACS Appl. Mater. Interfaces* **2018**, *10*, 32201–32211. [[CrossRef](#)]
29. Kumaravel, S.; Karthick, K.; Thiruvengadam, P.; Johnny, J.M.; Sankar, S.S.; Kundu, S. Tuning Cu Overvoltage for a Copper-Telluride System in Electrocatalytic Water Reduction and Feasible Feedstock Conversion: A New Approach. *Inorg. Chem.* **2020**, *59*, 11129–11141. [[CrossRef](#)]
30. Ghosh, A.; Mitra, M.; Banerjee, D.; Mondal, A. Facile Electrochemical Deposition of Cu_7Te_4 Thin Films with Visible-Light Driven Photocatalytic Activity and Thermoelectric Performance. *RSC Adv.* **2016**, *6*, 22803–22811. [[CrossRef](#)]
31. Wang, R.; Liu, Y.; Tian, Z.; Shi, Y.; Xu, Q.; Zhang, G.; Chen, J.; Zheng, W. Copper Telluride Nanosheet/ Cu Foil Electrode: Facile Ionic Liquid-Assisted Synthesis and Efficient Oxygen Evolution Performance. *J. Phys. Chem. C* **2020**, *124*, 22117–22126. [[CrossRef](#)]
32. Lee, D.J.; Mohan Kumar, G.; Ilanchezhian, P.; Xiao, F.; Yuldashev, S.U.; Woo, Y.D.; Kim, D.Y.; Kang, T.W. Arrayed CdTe Microdots and Their Enhanced Photodetectivity via Piezo-Phototronic Effect. *Nanomaterials* **2019**, *9*, 178. [[CrossRef](#)] [[PubMed](#)]
33. Lee, D.J.; Lee, Y.; Kwon, Y.H.; Choi, S.H.; Yang, W.; Kim, D.Y.; Lee, S. Room-Temperature Ferromagnetic Ultrathin $\alpha\text{-MoO}_3$: Te Nanoflakes. *ACS Nano* **2019**, *13*, 8717–8724. [[CrossRef](#)] [[PubMed](#)]
34. Salmón-Gamboa, J.U.; Barajas-Aguilar, A.H.; Ruiz-Ortega, L.L.; Garay-Tapia, A.M.; Jiménez-Sandoval, S.J. Vibrational and Electrical Properties of Cu_{2-x}Te films: Experimental Data and First Principle Calculations. *Sci. Rep.* **2018**, *8*, 8093. [[CrossRef](#)] [[PubMed](#)]
35. Pandey, J.; Mukherjee, S.; Rawat, D.; Athar, S.; Rana, K.S.; Mallik, R.C.; Soni, A. Raman Spectroscopy Study of Phonon Liquid Electron Crystal in Copper Deficient Superionic Thermoelectric Cu_{2-x}Te . *ACS Appl. Energy Mater.* **2020**, *3*, 2175–2181. [[CrossRef](#)]
36. Li, Q.; Rao, H.; Ma, X.; Mei, H.; Zhao, Z.; Gong, W.; Camposo, A.; Pisignano, D.; Yang, X. Unusual Red Light Emission from Nonmetallic Cu_2Te Microdisk for Laser and SERS Applications. *Adv. Opt. Mater.* **2022**, *10*, 2101976. [[CrossRef](#)]
37. He, L.; Zhou, D.; Lin, Y.; Ge, R.; Hou, X.; Sun, X.; Zheng, C. Ultrarapid In Situ Synthesis of Cu_2S Nanosheet Arrays on Copper Foam with Room-Temperature-Active Iodine Plasma for Efficient and Cost-Effective Oxygen Evolution. *ACS Catal.* **2018**, *8*, 3859–3864. [[CrossRef](#)]
38. Li, Z.; Zhang, Z. Tetrafunctional Cu_2S Thin Layers on Cu_2O Nanowires for Efficient Photoelectrochemical Water Splitting. *Nano Res.* **2018**, *11*, 1530–1540. [[CrossRef](#)]
39. Qian, K.; Gao, L.; Li, H.; Zhang, S.; Yang, J.; Liu, C.; Wang, J.; Qian, T.; Ding, H.; Zhang, Y.; et al. Epitaxial growth and air-stability of monolayer Cu_2Te . *Chin. Phys. B* **2020**, *29*, 018104. [[CrossRef](#)]
40. Jung, K.; Lim, T.; Bae, H.; Ha, J.S.; Martinez-Morales, A.A. Cu_2O Photocathode with Faster Charge Transfer by Fully Reacted Cu Seed Layer to Enhance Performance of Hydrogen Evolution in Solar Water Splitting Applications. *ChemCatChem* **2019**, *11*, 4377–4382. [[CrossRef](#)]
41. Farag, B.S.; Khodier, S.A. Direct and Indirect Transitions in Copper Telluride Thin Films. *Thin Solid Films* **1991**, *201*, 231–240. [[CrossRef](#)]
42. Caballero-Briones, F.; Palacios-Padrós, A.; Peña, J.L.; Sanz, F. Phase tailored, potentiodynamically grown $\text{p-Cu}_{2-x}\text{Te}/\text{Cu}$ layers. *Electrochem. Commun.* **2008**, *10*, 1684–1687. [[CrossRef](#)]
43. Dai, P.; Li, W.; Xie, J.; He, Y.; Thorne, J.; McMahon, G.; Zhan, J.; Wang, D. Forming Buried Junctions to Enhance the Photovoltage Generated by Cuprous Oxide in Aqueous Solutions. *Angew. Chem. Int. Ed.* **2014**, *53*, 13493–13497. [[CrossRef](#)] [[PubMed](#)]
44. Wang, P.; Ng, Y.H.; Amal, R. Embedment of anodized p-type Cu_2O thin films with CuO nanowires for improvement in photoelectrochemical stability. *Nanoscale* **2013**, *5*, 2952–2958. [[CrossRef](#)]
45. Kim, S.; Kim, H. Cu_2O Thin Film Photoelectrode Embedded with CuO Nanorods for Photoelectrochemical Water Oxidation. *J. Korean Inst. Surf. Eng.* **2019**, *5*, 258–264.
46. Chen, L.; Shet, S.; Tang, H.; Wang, H.; Deutsch, T.; Yan, Y.; Turner, J.; Al-Jassim, M. Electrochemical deposition of copper oxide nanowires for photoelectrochemical applications. *J. Mater. Chem.* **2010**, *20*, 6962–6967. [[CrossRef](#)]